STM JOURNALS

Journal of
Polymer & Composites

ISSN: 2321-2810 (Online)
ISSN: 2321-8525 (Print)
Volume 14, Special Issue 4, 2026
January–December
DOI (Journal): 10.37591/JoPC

https://journals.stmjournals.com/jopc

Research JoPC

Structural, Optical, Surface, and Gas-Sensing Properties of rGO/$Sn_{1-x}Zn_xO_2$ Nanocomposites

Shaikh Mohd. Waseem[1], Shahebaz S. Khan[1], Mahesh D. Raut[1], Kranti R. Zakde[2], Nikesh Kumar N. Ingle[3,*]

Abstract

rGO/$Sn_{1-x}Zn_xO_2$ nanocomposites with x = 0.00–0.75 were synthesized by sol–gel auto-combustion followed by wet impregnation with reduced graphene oxide. The adopted synthesis route enabled homogeneous Zn incorporation into the SnO_2 matrix and uniform distribution of rGO, leading to improved structural integrity and interfacial contact between the two components. XRD confirmed a dominant tetragonal cassiterite SnO_2 structure, while FTIR, FESEM, EDS, UV–visible, and BET analyses verified oxide–rGO coupling, Zn-dependent structural modification, porous morphology, and band-gap narrowing. The combined structural, compositional, optical, and surface analyses revealed that Zn substitution effectively altered the physicochemical properties of SnO_2 without generating undesirable secondary phases. The x = 0.45 composition exhibited the most favorable balance of crystallite size, defect density, nanoparticle dispersion, surface area, and pore volume, and was, therefore, selected for gas sensing. At 200°C and 100 ppm, the sensor showed responses of 99.36% to acetone, 98.51% to H_2S, and 35.86% to ethanol. H_2S produced the fastest response among the three gases, whereas acetone showed the most complete recovery. The enhanced behavior is attributed to chemisorbed oxygen reactions, Zn-associated defect sites, mesoporosity, and rGO-assisted interfacial charge transport. The synergistic interaction between Zn-doped SnO_2 and the conductive rGO network facilitates efficient electron transport, provides abundant active adsorption sites, and promotes rapid surface reactions with target gas molecules, thereby improving sensing characteristics. These results demonstrate its potential as a multigas chemoresistive platform for environmental and industrial monitoring.

Keywords: rGO, Zn-modified SnO_2, acetone sensing, mesoporosity, chemoresistive sensor

***Author for Correspondence**
Nikesh Kumar N. Ingle
E-mail: ningle@mgmu.ac.in

[1]Research Scholar, Department of Physics, School of Basic and Applied Sciences, MGM University, Chhatrapati Sambhaji Nagar, Maharashtra, India
[2]Associate Professor, Department of Physics, School of Basic and Applied Sciences, MGM University, Chhatrapati Sambhaji Nagar, Maharashtra, India
[3]Assistant Professor, Department of Physics, School of Basic and Applied Sciences, MGM University, Chhatrapati Sambhaji Nagar, Maharashtra, India

Received Date: July 06, 2026
Accepted Date: July 28, 2026
Published Date: August 17, 2026

Citation: Shaikh Mohd. Waseem, Shahebaz S. Khan, Mahesh D. Raut, Kranti R. Zakde, Nikesh Kumar N. Ingle. Structural, Optical, Surface, and Gas-Sensing Properties of rGO/$Sn_{1-x}ZnxO_2$ Nanocomposites. Journal of Polymer & Composites. 2026; 14(Special Issue 4): S429–S452p.

INTRODUCTION

Rapid industrial development, intensive fuel combustion, and the extensive use of solvent-based chemicals have increased the release of volatile organic compounds and toxic gases into indoor and outdoor environments. Ethanol vapor is generated in chemical processing, pharmaceutical production, food industries, fermentation units, and fuel-handling facilities, while prolonged exposure at elevated concentrations can cause irritation, impaired coordination, and occupational safety concerns. Acetone is extensively used in laboratories, polymer processing, painting, cleaning, and pharmaceutical manufacturing, and its concentration in exhaled breath has also been explored as a potential indicator of altered lipid metabolism and diabetes [1]. Hydrogen sulfide is a highly toxic and flammable gas released during petroleum refining, wastewater treatment, sewage decomposition, natural-gas processing,

and several sulfur-containing industrial operations. Exposure to low H_2S concentrations can damage the respiratory and nervous systems, while high concentrations may cause rapid unconsciousness and fatal poisoning [2]. These concerns have created a strong demand for compact chemoresistive sensors capable of detecting ethanol, acetone, and H_2S with high response, rapid reversibility, stable operation, and acceptable gas discrimination [3].

Semiconducting metal oxides remain among the most practical sensing materials because they combine chemical stability, scalable synthesis, straightforward resistance-based signal acquisition, and compatibility with miniaturized sensor platforms. Tin dioxide is particularly attractive because tetragonal SnO_2 is an intrinsically n-type semiconductor whose electrical conductivity is strongly influenced by surface oxygen adsorption. In air, oxygen molecules adsorb on the SnO_2 surface and extract conduction-band electrons, forming chemisorbed oxygen species and an electron-depletion region around individual crystallite. Interaction with a reducing gas returns electrons to the semiconductor, contracts the depletion layer, lowers the grain-boundary potential barrier, and decreases resistance. Consequently, the sensing signal is governed by the extent of surface-charge modulation, crystallite dimensions, accessible adsorption sites, and gas diffusion throughout the sensing film [4]. Despite these advantages, pristine SnO_2 commonly requires elevated operating temperatures to activate oxygen chemisorption and surface reactions. Nanoparticle agglomeration reduces accessible surface area, while similar surface reactions produced by different reducing gases lead to cross-sensitivity and inadequate molecular selectivity. These limitations increase power consumption and restrict the direct use of unmodified SnO_2 in portable sensing systems [3].

Aliovalent modification provides an effective route for regulating the crystal growth, defect chemistry, carrier density, and surface reactivity of SnO_2. Incorporation of divalent Zn^{2+} into a tetravalent Sn^{4+}-containing lattice can generate local charge imbalance, which may be compensated through oxygen-vacancy formation, electronic redistribution, and structural relaxation. The resulting lattice disorder can suppress crystallite growth by disturbing long-range atomic ordering and limiting grain-boundary migration during thermal treatment. Smaller crystallites provide a higher surface-to-volume ratio, while oxygen-deficient regions can promote oxygen chemisorption and strengthen interaction with target molecules. Zn incorporation may also alter the local electronic structure and adsorption energy of gas molecules, thereby changing the operating temperature, baseline resistance, and gas selectivity. Nevertheless, a small XRD peak displacement alone cannot establish substitutional incorporation of Zn^{2+}. Reliable interpretation requires supporting evidence from compositional analysis, X-ray photoelectron spectroscopy, X-ray absorption measurements, elemental mapping, lattice-parameter evolution, and the absence of detectable Zn-rich secondary phases. These effects are consistent with reported structural and surface changes in Zn-modified SnO_2 [3] and first-principles predictions for Zn-doped SnO_2 nanowires [5].

The integration of SnO_2 with reduced graphene oxide offers a complementary strategy for overcoming slow charge transfer and severe oxide-particle agglomeration. The partially restored sp^2-carbon framework of rGO provides interconnected conductive pathways that can lower charge-transfer resistance and facilitate rapid transport of electrons generated during surface reactions. Wrinkled rGO sheets also act as anchoring substrates for oxide nanoparticles, restricting particle coalescence and maintaining a porous architecture with exposed adsorption sites. Residual oxygen-containing functional groups on rGO support nanoparticle nucleation and provide additional binding sites for gas molecules. Contact between rGO and n-type SnO_2 produces electronically coupled heterointerfaces at which redistribution of charge modifies the interfacial potential barrier and amplifies resistance changes during adsorption and desorption [6]. Recent studies of rGO–metal oxide nanocomposites have demonstrated that heterointerface engineering can improve sensitivity, shorten response–recovery periods, and enable sensing at reduced temperature [7]. An et al. reported that an optimized rGO fraction improved the low-temperature ethanol-sensing performance of rGO/SnO_2 nanocomposites [2]. The rGO content must, however, be carefully controlled because excessive loading may cover oxide-active sites and form highly conductive parallel pathways, reducing the relative resistance modulation generated by the target

gas. The importance of carbon–SnO_2 interfaces for acetone and ethanol detection has also been reinforced by recent conductive carbon/SnO_2 sensing systems [8, 9]. Metal–oxide heterojunction strategies for ethanol sensing have also been reviewed extensively [10].

Although Zn-modified SnO_2 and rGO-supported metal oxides have individually received considerable attention, limited work has systematically connected Zn concentration, oxide crystallite evolution, rGO-supported nanoparticle distribution, mesoporosity, optical behavior, defect chemistry, and multi-gas sensing within a single compositionally controlled SnO_2 series. Most reported studies focus on one dopant concentration, one target gas, or a direct comparison between pristine and modified SnO_2. Such approaches do not fully explain why an intermediate dopant level can outperform both lower and higher concentrations. Excessive Zn addition may increase disorder while simultaneously promoting particle clustering, pore blockage, secondary-phase formation, and carrier trapping. Similarly, enhanced rGO conductivity does not necessarily produce a proportionate increase in sensing response when oxide–gas interactions become limited. Establishing a composition–structure–surface–sensing relationship is, therefore, necessary to distinguish the beneficial contributions of crystallite-size reduction, oxygen-vacancy generation, mesoporous diffusion, and interfacial electron transport from the detrimental effects associated with excessive structural disorder and agglomeration.

Accordingly, rGO/$Sn_{1-x}Zn_xO_2$ nanocomposites with six Zn concentrations, x = 0.00, 0.15, 0.30, 0.45, 0.60, and 0.75, were synthesized using a sol–gel auto-combustion route followed by wet impregnation with a fixed rGO loading. The composition-dependent evolution of crystal structure, metal–oxygen bonding, surface morphology, elemental composition, optical band gap, specific surface area, pore volume, and pore-size distribution was systematically examined. Particular attention was given to correlating Zn-induced structural defects and rGO-assisted interfacial transport with the resistance modulation produced during gas exposure. Among the investigated compositions, rGO/$Sn_{0.55}Zn_{0.45}O_2$ was selected for detailed sensing evaluation because it provided the most favorable balance of reduced crystallite size, defect concentration, nanoparticle dispersion, mesoporosity, accessible surface area, and rGO–oxide interfacial contact. Its chemoresistive behavior toward ethanol, acetone, and H_2S was investigated to establish dynamic response, selectivity, and response–recovery characteristics. The novelty lies in the systematic integration of composition control, defect regulation, mesoporous surface engineering, and graphene-assisted charge transport to explain the multigas sensing performance of an rGO-supported Zn-modified SnO_2 series.

EXPERIMENTAL

Materials

Tin(IV) chloride pentahydrate ($SnCl_4 \cdot 5H_2O$, ≥99%, Sigma-Aldrich), zinc nitrate hexahydrate ($Zn(NO_3)_2 \cdot 6H_2O$, ≥99%, Merck), urea (CH_4N_2O, ≥99%, Sigma-Aldrich), natural graphite powder (99.9%, Alfa Aesar), sulfuric acid (H_2SO_4, 98%), potassium permanganate ($KMnO_4$, ≥99%), hydrogen peroxide (H_2O_2, 30%), and hydrazine hydrate ($N_2H_4 \cdot H_2O$, 80%, Loba Chemie) were used as received without further purification. All solutions were prepared in double-distilled water.

Synthesis of Graphene Oxide (GO)

Graphene oxide was synthesized from natural graphite powder by a modified Hummers method [11]. Graphite powder (2 g) was added to concentrated H_2SO_4 (46 mL) under ice-bath cooling and continuous stirring. $KMnO_4$ (6 g) was then added slowly in small portions while maintaining the temperature below 10°C. The mixture was subsequently stirred at 35°C for 2 h, after which distilled water (92 mL) was added carefully and the temperature was raised to 98°C for a further 30 min. The reaction was terminated by addition of H_2O_2 solution (140 mL, 5%) until no further gas evolution was observed. The resulting suspension was filtered and washed repeatedly with dilute HCl (5%) and distilled water until the filtrate reached neutral pH. The product was dried at 60°C for 24 h to yield GO powder.

Synthesis of Reduced Graphene Oxide (rGO)

Reduction of GO to rGO was carried out by chemical reduction with hydrazine hydrate. GO powder (200 mg) was dispersed in distilled water (200 mL) by ultrasonication for 1 h to obtain a stable suspension. Hydrazine hydrate (2 mL) was added dropwise under continuous stirring, and the suspension was heated at 95°C for 12 h. The black precipitate was collected by filtration, washed with distilled water and ethanol several times, and dried at 80°C for 12 h. The resulting rGO powder was stored in a desiccator until use.

Synthesis of $Sn_{1-x}Zn_xO_2$ Nanoparticles

$Sn_{1-x}Zn_xO_2$ nanoparticles (x = 0.00, 0.15, 0.30, 0.45, 0.60, 0.75) were prepared by a sol–gel auto-combustion method. Stoichiometric amounts of $SnCl_4 \cdot 5H_2O$ and $Zn(NO_3)_2 \cdot 6H_2O$ were dissolved together in distilled water (50 mL) under magnetic stirring to obtain a clear mixed-precursor solution. Urea was added as a fuel in a molar ratio of fuel to total metal nitrate of 3:1. The solution was stirred at 80°C until a viscous gel formed, then transferred to a preheated muffle furnace at 300°C. The gel underwent self-ignition and combustion within a few minutes, yielding a loose, porous as-burnt powder. The powder was ground in an agate mortar and calcined at 500°C for 4 h in air at a heating rate of 5°C min^{-1} to remove residual organic matter and improve crystallinity. The calcined powders are denoted SZO-0, SZO-15, SZO-30, SZO-45, SZO-60, and SZO-75 corresponding to x = 0.00–0.75.

Synthesis of rGO/$Sn_{1-x}Zn_xO_2$ Nanocomposites

rGO/$Sn_{1-x}Zn_xO_2$ nanocomposites were prepared by a wet impregnation method. rGO powder (10 wt% relative to the oxide) was dispersed in ethanol (30 mL) by ultrasonication for 30 min to form a uniform suspension. The appropriate $Sn_{1-x}Zn_xO_2$ powder was then added, and the mixture was sonicated for a further 1 h, followed by magnetic stirring at 60°C until the solvent evaporated completely. The dry composite powder was annealed at 250°C for 2 h in an argon atmosphere to promote interfacial contact between rGO and the oxide phase without thermally degrading the graphene network. The six composites are designated rGO/SZO-0, rGO/SZO-15, rGO/SZO-30, rGO/SZO-45, rGO/SZO-60, and rGO/SZO-75.

Characterization

The crystal structure and phase purity of all samples were determined by X-ray diffraction (XRD) using a Bruker D8 Advance diffractometer with Cu Kα radiation (λ = 1.5406 Å) over a 2θ range of 10°–80° at a scan rate of 2° min^{-1}. Crystallite size, microstrain, and dislocation density were calculated from the Debye–Scherrer equation and strain formula. Fourier-transform infrared (FTIR) spectra were recorded on a PerkinElmer Spectrum Two spectrometer in the range 400–4000 cm^{-1} using the KBr pellet method. Surface morphology and elemental composition were examined by field-emission scanning electron microscopy (FESEM) with energy-dispersive X-ray spectroscopy (EDS) on a JEOL JSM-7600F instrument operated at 15 kV. Optical absorption spectra were measured on a Shimadzu UV-2600 UV–visible spectrophotometer over 200–800 nm; optical band gaps were estimated from Tauc plots assuming direct-allowed transitions. Specific surface area, pore volume, and average pore diameter were determined by N_2 adsorption–desorption at 77 K on a Micromeritics ASAP 2020 instrument; surface area was calculated by the Brunauer–Emmett–Teller (BET) method and pore-size distribution by the Barrett–Joyner – Halenda (BJH) method. All samples were degassed at 150°C for 6 h prior to BET measurement.

Sensor Fabrication

For sensor fabrication, each rGO/$Sn_{1-x}Zn_xO_2$ composite powder was mixed with a small volume of deionized water to form a homogeneous, viscous paste. The paste was deposited onto alumina substrates (10 mm × 10 mm) pre-patterned with silver interdigitated electrodes by the doctor-blade technique, using a blade gap set to produce a wet-film thickness of upto 200 μm. The coated substrates were dried at 80°C for 1 h to remove residual solvent and then annealed at 300°C for 2 h in air to improve film adhesion and stabilize the sensing layer. Electrical contacts were established by applying conducting silver paste to the electrode terminals and curing at 120°C for 30 min. The fabricated sensors were

mounted inside a sealed stainless-steel test chamber equipped with electrical feedthroughs, gas inlet and outlet ports, and a PID-controlled heater.

Gas-Sensing Measurements

The gas-sensing behavior of rGO/$Sn_{1-x}Zn_xO_2$ sensors was evaluated toward ethanol, acetone, and H_2S. Prior to each measurement, the sensor was stabilized in dry air at the selected operating temperature until a steady baseline resistance (R_a) was achieved, typically within 10–15 min. A calibrated concentration of target gas (5–500 ppm) was then introduced into the test chamber at a total flow of 200 sccm using mass-flow controllers, and the change in sensor resistance was recorded continuously as a function of time using a Keithley 2400 source-meter under a constant bias of 1 V, connected to a computer-controlled data acquisition system. After gas exposure, the chamber was purged with dry air to allow resistance recovery. The gas response was defined as $S\ (\%) = [(R_a - Rg)/R_a] \times 100$ for the investigated reducing gases, where R_a and Rg are the resistance in air and in the target gas, respectively. Response time (tres) and recovery time (trec) were defined as the times required for the resistance to reach 90% of its total change upon gas introduction and upon return to air, respectively. All measurements were performed in triplicate and mean values are reported.

RESULTS AND DISCUSSION

XRD Analysis

Figure 1 compares the X-ray diffraction patterns of pure rGO, $Sn_{1-x}Zn_xO_2$ nanoparticles, and rGO/$Sn_{1-x}Zn_xO_2$ nanocomposites with x = 0.00, 0.15, 0.30, 0.45, 0.60, and 0.75. The diffraction profiles of the oxide and composite samples are dominated by reflections corresponding to tetragonal cassiterite SnO_2 with space group $P4_2/mnm$. The principal peaks observed at approximately 2θ = 26.61°, 33.89°, 37.95°, 51.78°, 54.76°, 57.82°, 61.87°, 64.72°, 65.94°, 71.28°, and 78.71° are indexed to the (110), (101), (200), (211), (220), (002), (310), (112), (301), (202), and (321) planes, respectively, in agreement with JCPDS No. 41-1445. These reflections confirm that cassiterite-type SnO_2 is the dominant crystalline structure throughout the investigated composition range.

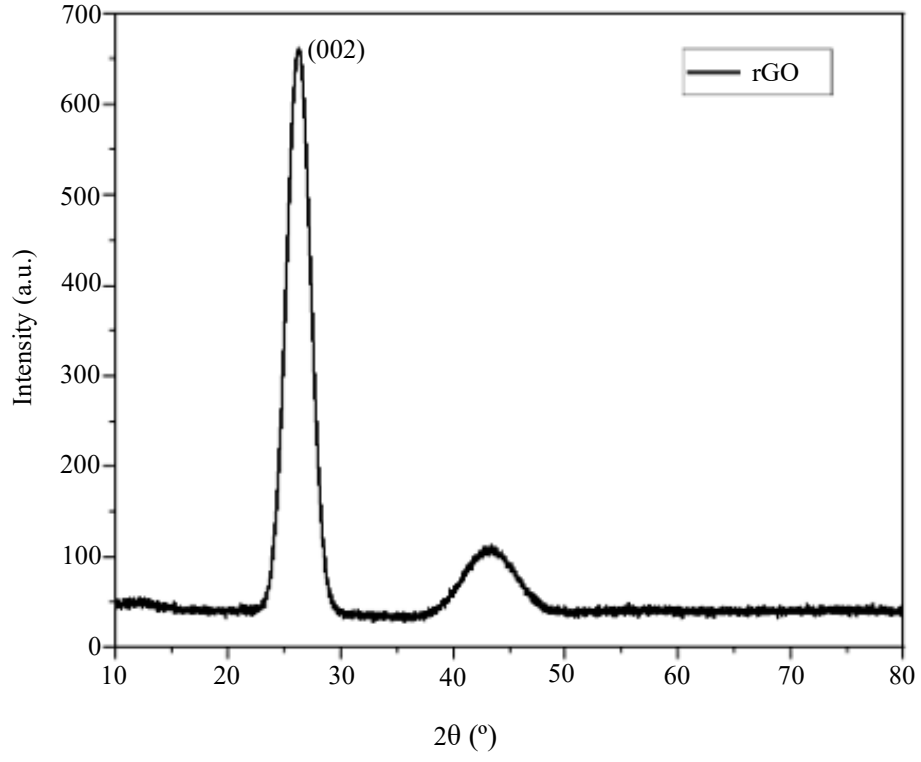

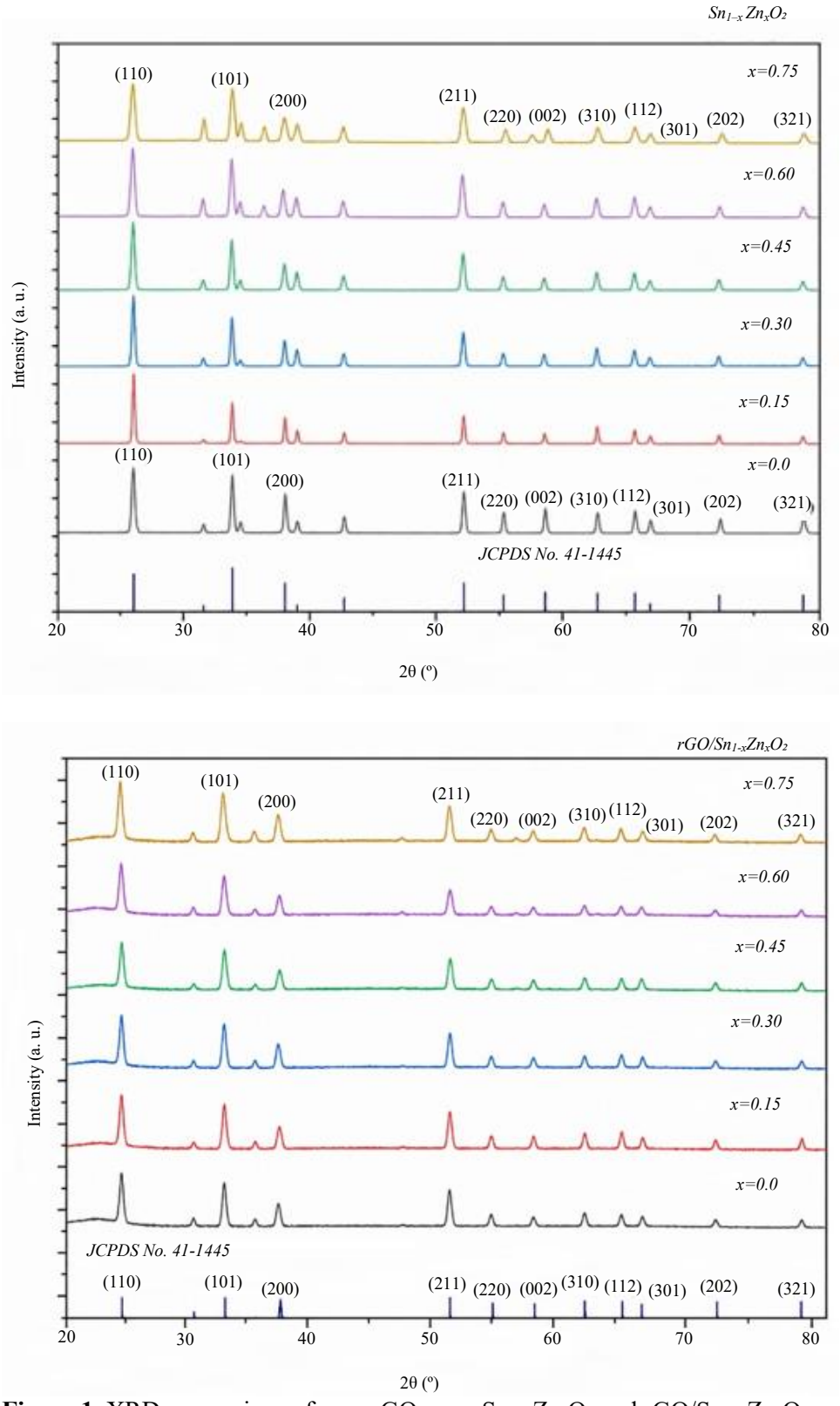

Figure 1. XRD comparison of pure rGO, pure $Sn_{1-x}Zn_xO_2$ and rGO/$Sn_{1-x}Zn_xO_2$.

No clearly resolved diffraction peaks corresponding to crystalline ZnO, Zn_2SnO_4, metallic Zn, SnO, or other secondary compounds are detected within the sensitivity of laboratory XRD. However, the absence of separate impurity reflections cannot independently establish complete substitutional

incorporation of Zn^{2+} into the SnO_2 lattice. Highly dispersed Zn-containing domains, amorphous phases, and minor secondary phases may remain below the XRD detection limit. Therefore, the samples should be described as having a dominant tetragonal SnO_2 structure rather than as conclusively single phase without Rietveld refinement, XPS, HRTEM, or local-structure evidence. More broadly, structure–activity relationships in SnO_2 depend strongly on its local structure and surface state [12].

Pure rGO shows a broad graphitic contribution in the 2θ region of approximately 24–27°, generally attributed to the partially restored (002) stacking of sp^2-bonded carbon layers after reduction of graphene oxide. In the rGO/$Sn_{1-x}Zn_xO_2$ nanocomposites, this broad rGO feature overlaps with the intense SnO_2 (110) reflection near 26.6°. Therefore, the rGO contribution is not clearly resolved as an independent peak and may instead contribute to the broadening and asymmetry of the composite peak. Raman analysis is required to confirm the reduction of GO and evaluate the structural disorder of rGO through the D and G bands.

With increasing Zn content, the principal (110) reflection shifts gradually from 26.610° for x = 0.00 to 26.685° for x = 0.75. The corresponding interplanar spacing decreases from 3.347 to 3.338 Å. This systematic displacement toward higher diffraction angles indicates modification of the average SnO_2 lattice after Zn addition. The shift may arise from defect-assisted lattice relaxation, oxygen non-stoichiometry, local strain, surface stress, and changes in the metal–oxygen coordination environment. Nevertheless, peak shifting alone is insufficient to prove that Zn^{2+} occupies Sn^{4+} lattice sites. The interplanar spacing was calculated using Bragg's law:

$$n\lambda = 2d \sin\theta$$

where n is the diffraction order, λ is the wavelength of Cu Kα radiation, d is the interplanar spacing, and θ is the Bragg angle. For a tetragonal crystal structure, the lattice parameters are related to the interplanar spacing by:

$$\frac{1}{d^2} = \frac{h^2 + k^2}{a^2} + \frac{l^2}{c^2}$$

The unit-cell volume was determined using:

$$V = a^2 c$$

The lattice parameter a decreases from 4.734 Å for x = 0.00 to 4.721 Å for x = 0.75, while $c$decreases from 3.186 to 3.180 Å. Consequently, the unit-cell volume decreases from 71.384 to 70.858 $Å^3$. This small but systematic contraction agrees with the positive shift of the (110) reflection. The observed contraction may be associated with local defect compensation, oxygen-vacancy formation, structural relaxation around Zn-containing regions, and increasing internal strain. Reliable determination of both $a$and $c$should be based on several indexed reflections because the (110) peak alone cannot determine the $c$parameter. The average crystallite size was estimated using the Debye–Scherrer equation:

$$D = \frac{K\lambda}{\beta \cos\theta}$$

where D is the coherent crystallite size, K is the shape factor, λ is the X-ray wavelength, β is the full width at half maximum in radians, and θ is the Bragg angle. The microstrain was calculated from:

$$\varepsilon = \frac{\beta}{4 \tan\theta}$$

The dislocation density was obtained using:

$$\delta = \frac{1}{D^2}$$

The FWHM of the (110) reflection increases continuously from 0.2300° for x = 0.00 to 0.4400° for x = 0.75. Correspondingly, the crystallite size decreases from 35.49 to 18.56 nm. This reduction indicates that increasing Zn content suppresses coherent crystallite growth and introduces structural disorder into the SnO_2 framework. Zn-related defects can disturb the regular arrangement of Sn–O octahedra, limit grain-boundary migration, and increase the number of nucleation centres during synthesis and thermal treatment.

The microstrain increases from 4.24×10^{-3} to 8.09×10^{-3}, while the dislocation density rises from $0.794 \times 10^{15}$to $2.904 \times 10^{15}$$m^{-2}$. The simultaneous increase in FWHM, microstrain, and dislocation density confirms the progressive development of a more distorted and defect-rich oxide framework. The calculated crystallite sizes for x = 0.00, 0.15, 0.30, 0.45, 0.60, and 0.75 are 35.49, 30.01, 26.00, 22.93, 20.51, and 18.56 nm, respectively.

The rGO sheets can additionally influence crystallite growth by providing heterogeneous nucleation and anchoring sites for $Sn_{1-x}Zn_xO_2$ nanoparticles. Residual oxygen-containing groups and defect sites on the rGO surface promote attachment of oxide nuclei and spatially separate the growing crystallites. This effect can restrict nanoparticle coalescence and preserve smaller coherent domains. However, the broad rGO (002) contribution overlaps with the SnO_2 (110) reflection, and part of the measured peak broadening may arise from this overlap. A quantitative assessment of rGO-induced crystallite-growth suppression requires direct comparison between pure $Sn_{1-x}Zn_xO_2$ and rGO/$Sn_{1-x}Zn_xO_2$ samples prepared under identical conditions.

FTIR Analysis

Figure 2 shows the FTIR spectra of rGO/$Sn_{1-x}Zn_xO_2$ nanocomposites recorded in the range of 400–4000 cm^{-1}. The broad band near 3400–3450 cm^{-1} and the feature around 1620–1640 cm^{-1} are assigned to O–H stretching and H–O–H bending vibrations of surface hydroxyl groups and adsorbed moisture, respectively. Weak bands near 1720, 1380–1400, 1220, and 1050 cm^{-1} correspond to residual C=O, C–OH, C–O–C, and C–O groups of partially reduced graphene oxide. Their persistence indicates that a limited number of oxygen-containing functional groups remain on rGO and can act as anchoring sites for oxide nanoparticles.

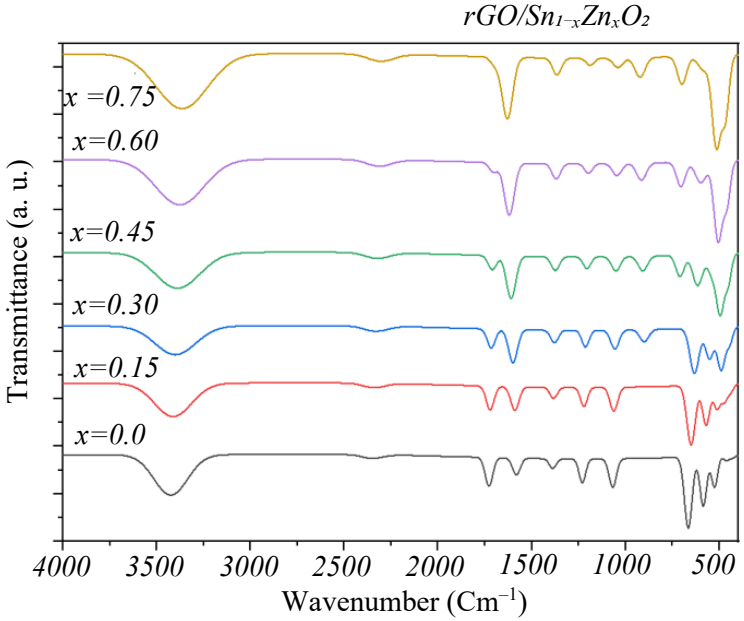

Figure 2. FTIR spectra of rGO/$Sn_{1-x}Zn_xO_2$ nanocomposites with x = 0.00–0.75.

The intense low-wavenumber bands around 600–650 and 520–580 cm^{-1} are associated with Sn–O–Sn and Sn–O vibrations of the cassiterite SnO_2 framework. With increasing Zn concentration, these bands broaden slightly and shift toward lower wavenumber, indicating modification of the local metal–oxygen bonding environment and increasing lattice disorder. A weak contribution near 450–500 cm^{-1} may arise from Zn–O and mixed Sn–O–Zn vibrations. However, FTIR alone cannot confirm substitutional Zn incorporation because Sn–O and Zn–O vibration ranges overlap considerably.

Comparable broadening and displacement of metal–oxygen bands were reported for Zn-modified SnO_2 nanoparticles and were attributed to Zn-induced local distortion of the SnO_2 network [3]. The coexistence of rGO-related oxygen functionalities and Sn–O lattice vibrations is also consistent with recent rGO/SnO_2 nanocomposites, in which residual functional groups improve nanoparticle anchoring and oxide–carbon interfacial contact [2]. The rGO/SZO-45 composition retains clearly identifiable metal–oxygen bands together with weak carbon-related features, supporting effective coupling between the oxide phase and rGO framework.

FESEM Analysis

Figure 3 shows the FESEM micrographs of rGO/$Sn_{1-x}Zn_xO_2$ nanocomposites with x = 0.00–0.75. The samples consist of irregular oxide nanoparticles distributed over wrinkled and fragmented rGO sheets, producing a rough and porous surface. The x = 0.00 sample shows comparatively larger agglomerates, whereas increasing Zn content progressively improves nanoparticle dispersion and reduces the apparent particle size up to x = 0.45. This behavior agrees with the XRD-derived reduction in crystallite size and suggests that Zn incorporation suppresses excessive oxide growth.

The rGO/SZO-45 sample displays the most uniform oxide distribution, interconnected voids, and extensive contact between the nanoparticles and rGO sheets. Such morphology provides more accessible adsorption sites and shorter gas-diffusion pathways while the rGO network supports rapid interfacial electron transport. At higher Zn contents, particularly x = 0.60 and 0.75, particle clustering and compact agglomerated regions become more evident, which may obstruct pores and reduce the accessible sensing surface.

An et al. reported a similar anchoring of SnO_2 nanoparticles on rGO sheets, where the carbon framework restricted particle aggregation and improved interfacial charge transfer for low-temperature ethanol sensing [2]. The Zn-dependent morphological variation is also consistent with reported Zn-modified SnO_2 systems, in which Zn addition altered nanoparticle growth, porosity, and gas-accessible surface structure [13]. Therefore, the comparatively homogeneous and porous morphology of rGO/SZO-45 supports its improved gas-sensing behavior, although quantitative particle-size analysis and TEM imaging are required for definitive confirmation.

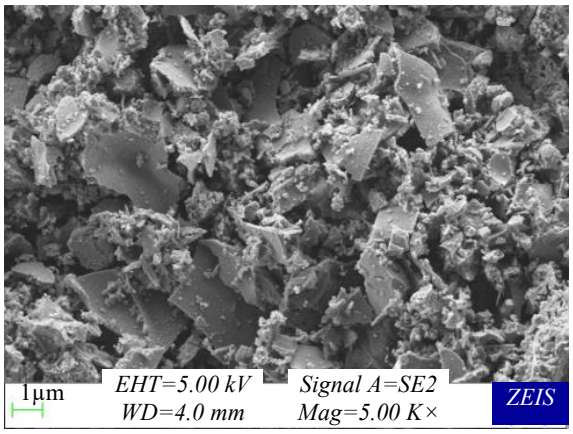

x=0.0

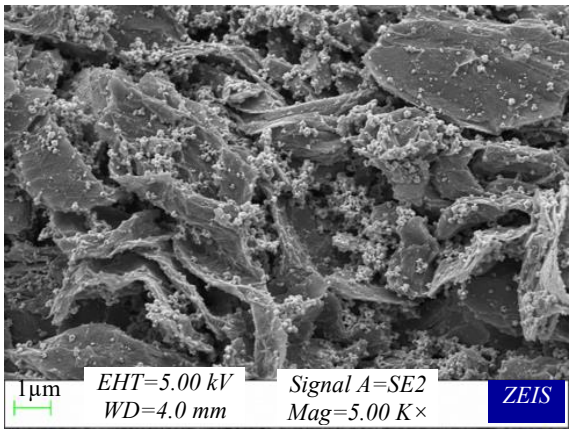

x=0.15

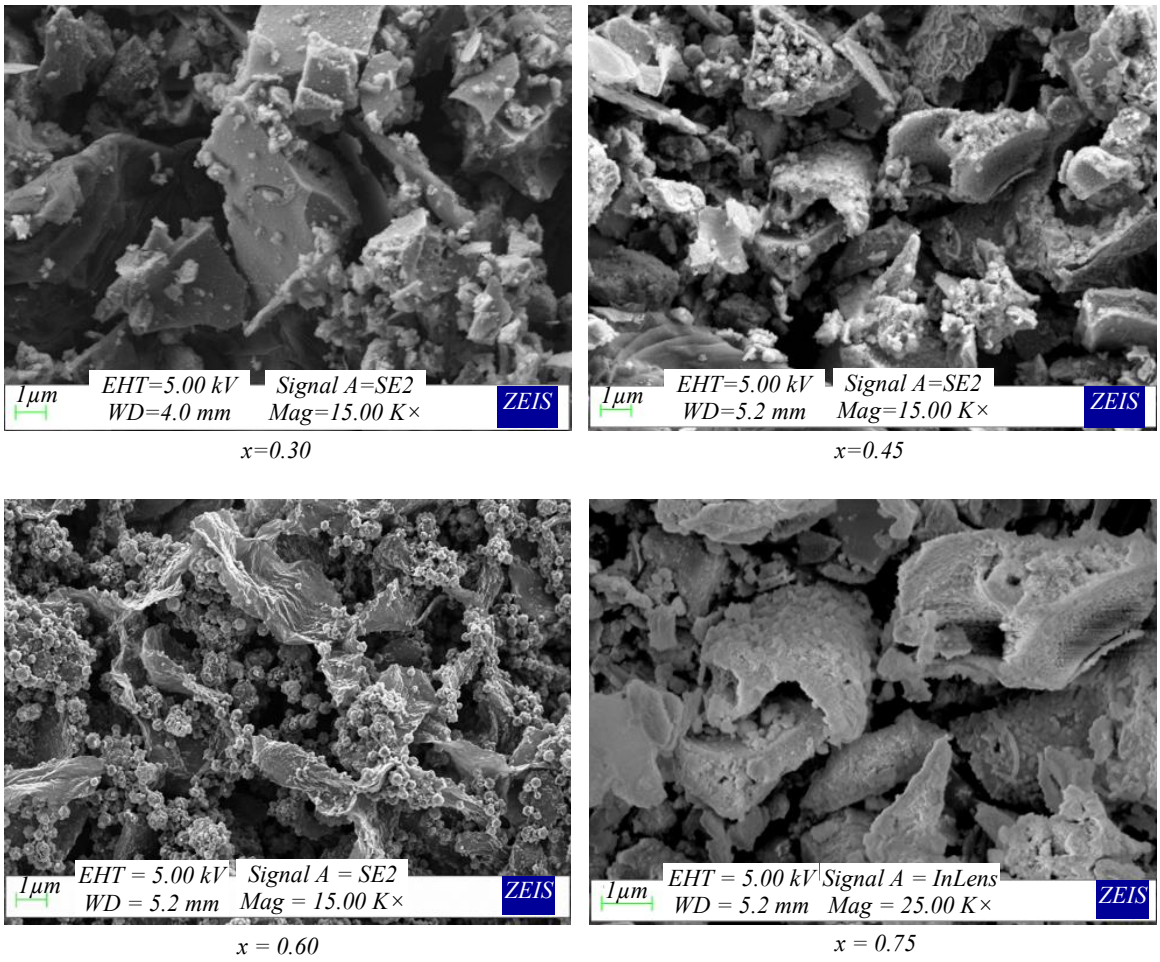

Figure 3. FESEM micrographs of rGO/$Sn_{1-x}Zn_xO_2$ nanocomposites.

EDS Analysis

Figure 4 presents the EDS spectra and quantitative elemental compositions of rGO/$Sn_{1-x}Zn_xO_2$ nanocomposites with x = 0.00–0.75. The spectra confirm the presence of C, O, Sn, and Zn without detectable signals from major precursor-derived contaminants. Carbon originates from the rGO framework, while Sn and O correspond to the SnO_2-based oxide phase. Zn peaks appear in all substituted samples and increase systematically with nominal Zn concentration.

The Zn weight percentage rises from 8.92% for x = 0.15 to 47.03% for x = 0.75, while the Sn content decreases from 58.9% to 22.18%. This opposite variation confirms successful compositional control across the series. The carbon content remains close to 9–10 wt%, which is consistent with the fixed rGO loading used during composite preparation. The x = 0.45 sample contains 9.35 wt% C, 22.18 wt% O, 40.73 wt% Sn, and 27.74 wt% Zn.

Similar Zn-dependent changes in elemental composition have been observed in Zn-modified SnO_2 nanocrystals, where EDS and elemental mapping confirmed the coexistence and spatial distribution of Sn, Zn, and O [3]. The retention of carbon together with oxide-related elements is also consistent with rGO/SnO_2 nanocomposites reported by An et al. [2].

EDS confirms elemental incorporation and approximate composition, but it does not establish the oxidation state, lattice position of Zn, oxygen-vacancy concentration, or phase purity. These aspects require XPS, HRTEM mapping, and structural refinement.

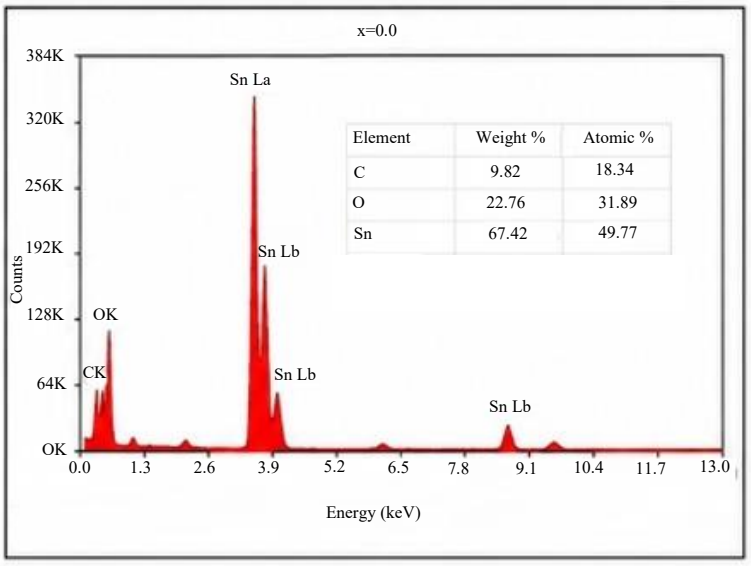

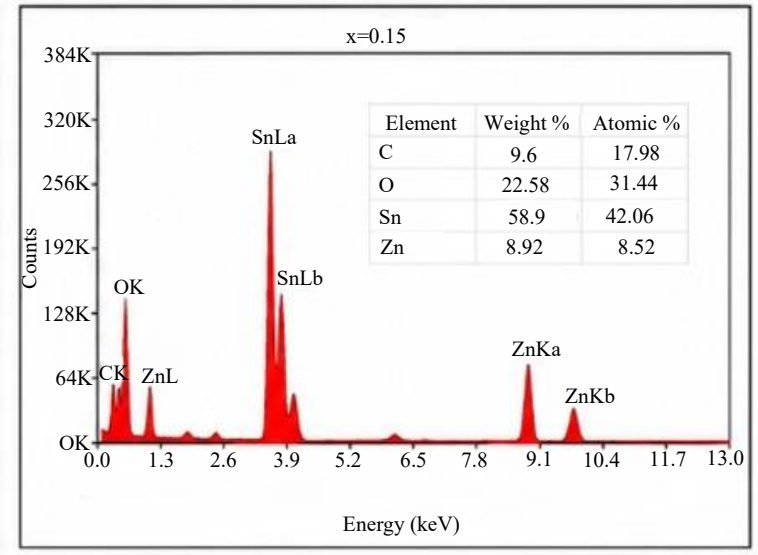

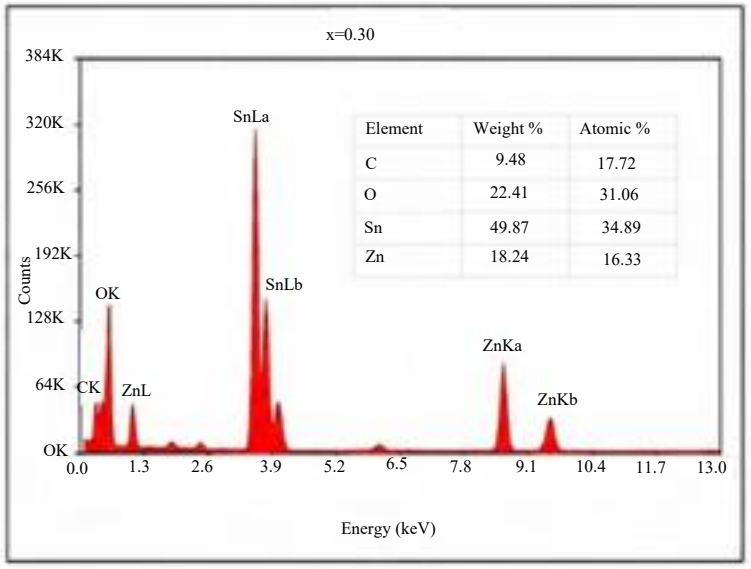

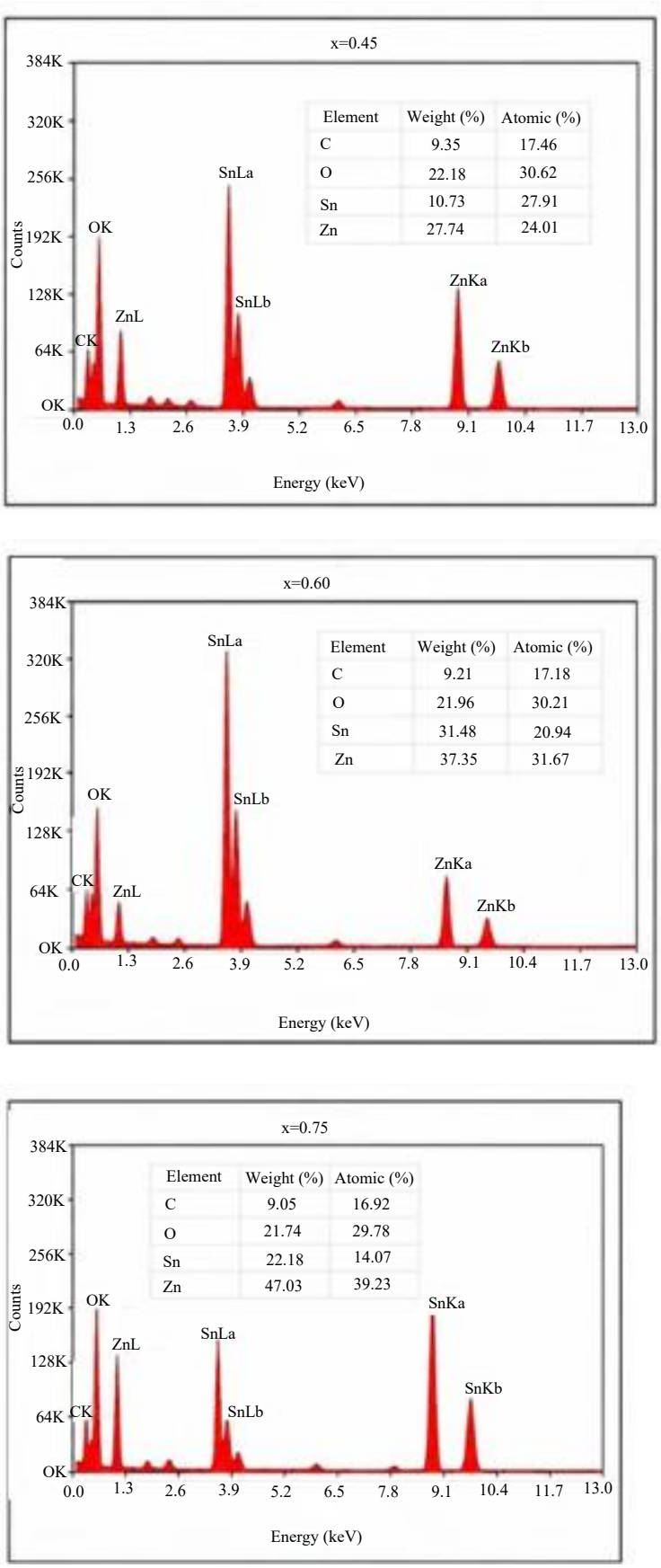

Figure 4. EDS spectrum of rGO/$Sn_{1-x}Zn_xO_2$ nanocomposites.

UV–Visible and Optical Band-Gap Analysis

Figure 5 shows the UV–visible absorption spectra and direct Tauc plots of rGO/$Sn_{1-x}Zn_xO_2$ nanocomposites. All samples exhibit strong absorption in the ultraviolet region, followed by a gradual decrease toward the visible region. The absorption edge shifts toward longer wavelengths with increasing Zn content, indicating modification of the electronic structure and progressive band-gap narrowing.

The optical band gap was determined using the direct-transition Tauc relation:

$$(\alpha h\nu)^2 = A(h\nu - E_g)$$

where α is the absorption coefficient, $h\nu$is the photon energy, $A$is a proportionality constant, and E_g is the optical band gap. The extrapolated band-gap values decrease from 3.32 eV for x = 0.00 to 3.24, 3.10, 2.96, 2.90, and 2.80 eV for x = 0.15, 0.30, 0.45, 0.60, and 0.75, respectively.

The decrease in $E_g$may arise from Zn-associated defect states, oxygen non-stoichiometry, lattice disorder, and electronic coupling between $Sn_{1-x}Zn_xO_2$ and rGO. Similar band-gap reduction with increasing Zn concentration was reported for Zn-doped SnO_2 nanostructures and attributed to defect-induced localized states within the forbidden-energy region [14]. Alanazi et al. also observed a reduction in the optical band gap of Zn-modified SnO_2 nanoparticles after Zn addition [15]. The rGO framework may further broaden visible-light absorption by introducing interfacial electronic states and promoting charge delocalization.

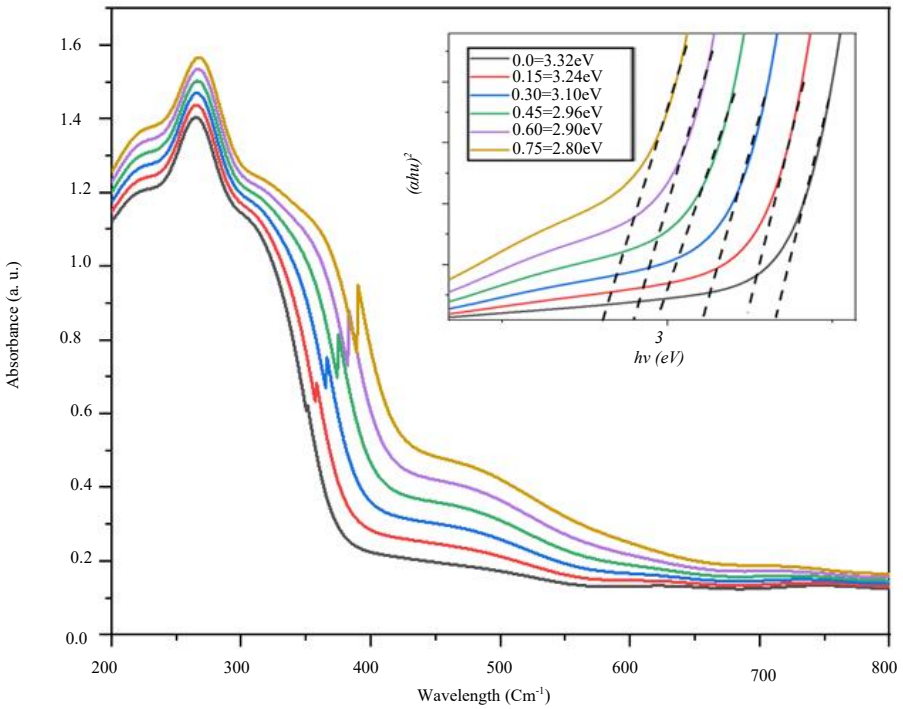

Figure 5. UV–visible absorption spectra. and direct Tauc plots of rGO/$Sn_{1-x}Zn_xO_2$ nanocomposites.

The x = 0.45 nanocomposite exhibits an intermediate band gap of 2.96 eV, providing a balance between easier carrier excitation and retention of sufficient semiconducting resistance modulation. Excessive narrowing at higher Zn contents may increase carrier trapping and structural disorder, which can explain why x = 0.75 does not necessarily provide the best sensing performance despite having the lowest optical band gap.

BET Surface Area and Porosity Analysis

Figure 6(a–f) shows the N_2 adsorption–desorption isotherms of rGO/$Sn_{1-x}Zn_xO_2$ nanocomposites measured at 77 K. All compositions exhibit type-IV isotherms with hysteresis loops, indicating mesoporous structures in which multilayer adsorption and capillary condensation occur within mesopores, consistent with the IUPAC classification [16].

The specific surface area was calculated using the Brunauer–Emmett–Teller equation:

$$\frac{P}{V(P_0 - P)} = \frac{1}{V_m C} + \frac{C - 1}{V_m C}\left(\frac{P}{P_0}\right)$$

where V is the adsorbed nitrogen volume, V_m is the monolayer capacity, C is the BET constant, and P/P_0 is the relative pressure. The pore volume and average pore diameter were evaluated using the Barrett–Joyner–Halenda method [17, 18].

The BET surface area increases from 64.8 $m^2\ g^{-1}$ for rGO/SZO-0 to a maximum of 168.2 $m^2\ g^{-1}$ for rGO/SZO-45. The corresponding pore volume increases from 0.155 to 0.485 $cm^3\ g^{-1}$, while the average pore diameter decreases from 12.6 to 6.9 nm.

These changes indicate the formation of a finer and more accessible mesoporous network up to x = 0.45. The improvement is attributed to suppression of crystallite growth, improved oxide dispersion over the rGO sheets, and reduced nanoparticle coalescence.

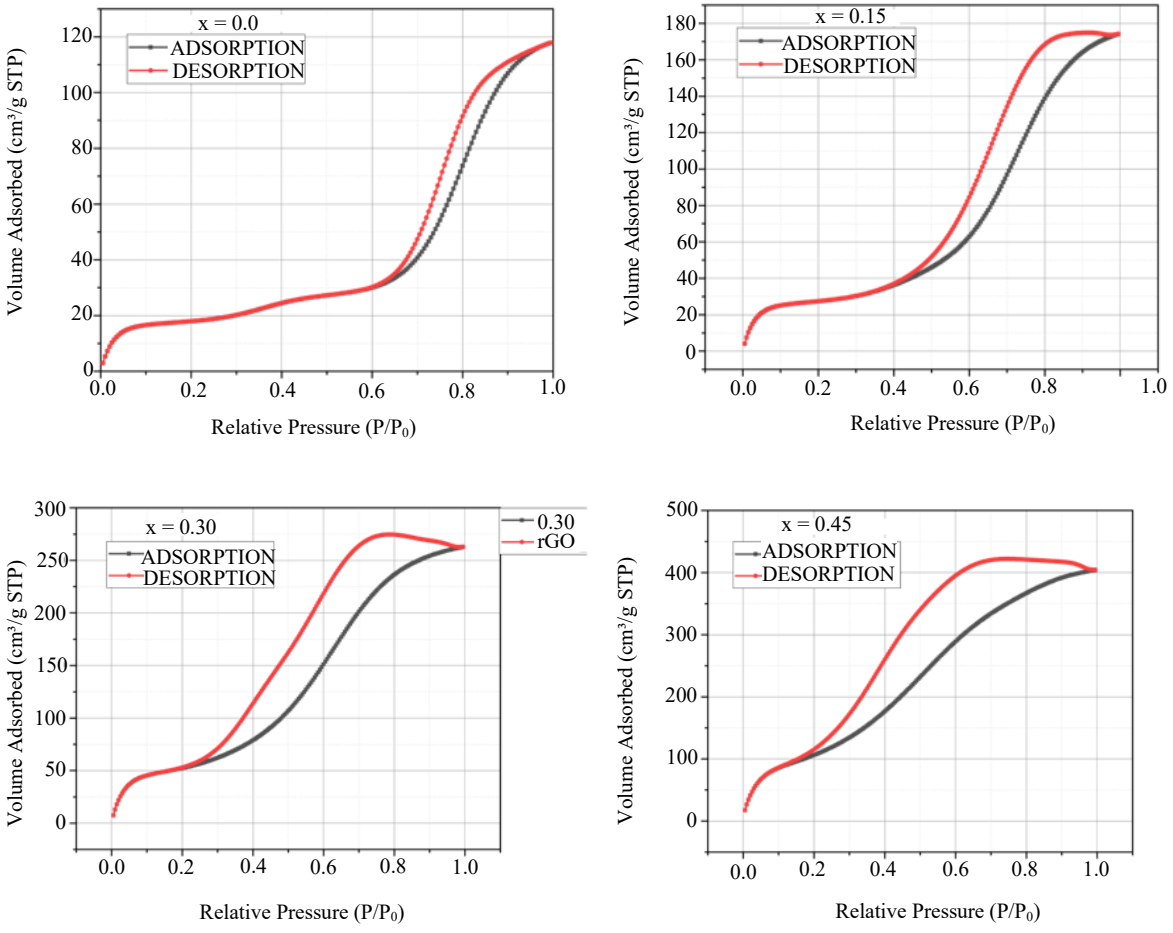

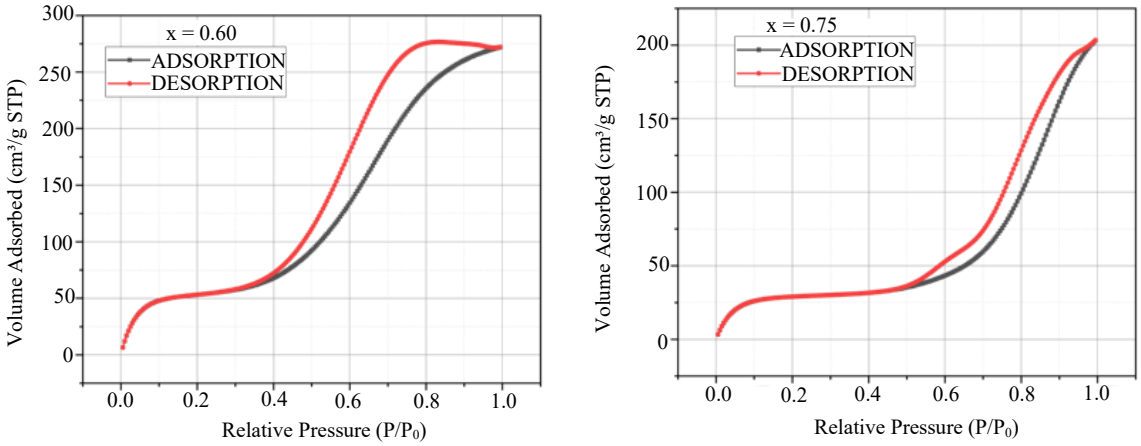

Figure 6. BET N_2 adsorption–desorption isotherms.

At higher Zn concentrations, the surface area decreases to 134.6 $m^2\ g^{-1}$ for x = 0.60 and 96.3 $m^2\ g^{-1}$ for x = 0.75. This reduction, together with the increase in average pore diameter, suggests particle clustering, partial pore blockage, and development of larger interparticle voids. Similar structure–property relationships have been reported for porous rGO–metal oxide sensing materials, where optimized porosity improves adsorption and gas diffusion, whereas excessive aggregation reduces the accessible active surface [19].

Among all compositions, rGO/SZO-45 exhibits the highest surface area, largest pore volume, and smallest average pore diameter. These characteristics provide abundant adsorption sites and short diffusion pathways for oxygen and target gas molecules. The porous structure, combined with the conductive rGO framework, is, therefore, expected to enhance surface reactions and charge transport during gas sensing. The BET and BJH parameters for all samples are summarized in Table 1.

Table 1. BET surface area, pore volume, and average pore diameter of rGO/$Sn_{1-x}Zn_xO_2$ nanocomposites.

x	BET surface area (m^2/g)	Pore volume (cm^3/g)	Avg. pore diameter (nm)
0.00	64.8	0.155	12.6
0.15	88.5	0.224	10.8
0.30	119.4	0.337	8.9
0.45	168.2	0.485	6.9
0.60	134.6	0.356	9.8
0.75	96.3	0.262	15.4

Gas-Sensing Performance

The gas-sensing performance of rGO/$Sn_{0.55}Zn_{0.45}O_2$ was evaluated toward 100 ppm acetone, ethanol, and H_2S at 200°C. Before each measurement, the sensor was stabilized in air to obtain a steady baseline resistance, followed by target-gas exposure and clean-air purging for recovery. The x = 0.45 composition was selected because it exhibited the highest BET surface area of 168.2 $m^2\ g^{-1}$, the largest pore volume of 0.485 $cm^3\ g^{-1}$, a reduced crystallite size of 22.93 nm, and comparatively uniform nanoparticle dispersion over the rGO sheets. These features provide abundant adsorption sites, facilitate gas diffusion, and support rapid charge transport through the conductive rGO network. Exposure to acetone, ethanol, and H_2S decreased the resistance through electron release from surface reactions.

Dynamic Resistance–Time Behavior

The dynamic resistance–time profiles of rGO/$Sn_{0.55}Zn_{0.45}O_2$ toward 100 ppm acetone, ethanol, and H_2S at 200°C reveal distinct gas-dependent electrical responses. The baseline resistances in air were 7.6236×10^{10}, 6.4856×10^{10}, and 1.4299×10^{11} Ω for acetone, ethanol, and H_2S, respectively. Upon

acetone exposure, the resistance decreased sharply to 4.8533×10^8 Ω, indicating strong interaction with chemisorbed oxygen species and substantial electron release into the conduction network. Ethanol produced a comparatively smaller resistance decrease to 4.1600×10^{10} Ω, reflecting weaker surface oxidation and slower charge-transfer kinetics. The corresponding dynamic resistance–time profiles are shown in Figure 7.

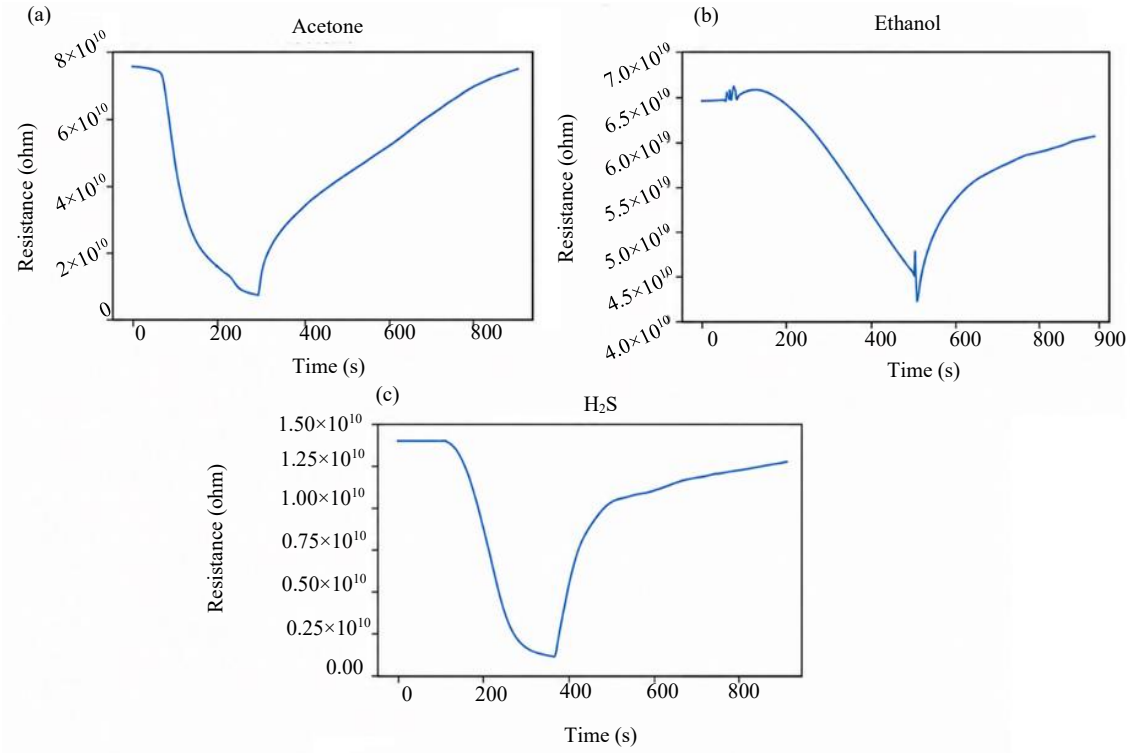

Figure 7. Dynamic resistance–time profiles of rGO/$Sn_{0.55}Zn_{0.45}O_2$.

H_2S exposure reduced the resistance to 2.1295×10^9 Ω, confirming its strong reactivity with ionized oxygen species and rapid electron return to the oxide–rGO network.

During clean-air purging, the acetone response approached its initial baseline, whereas ethanol and H_2S showed incomplete recovery within the recorded period. The observed resistance modulation arises from surface oxygen reactions, Zn-associated defect sites, rGO-assisted charge transport, and variation of the rGO/$Sn_{0.55}Zn_{0.45}O_2$ interfacial barrier.

Gas-Response Comparison and Selectivity

The gas response of rGO/$Sn_{0.55}Zn_{0.45}O_2$ toward 100 ppm acetone, ethanol, and H_2S at 200°C was calculated from the resistance measured in air (R_a) and in the target-gas atmosphere (Rg). For the investigated reducing gases, the response was determined using $S\ (\%) = [(R_a - Rg)/R_a] \times 100$.

The calculated responses were 99.36% for acetone, 35.86% for ethanol, and 98.51% for H_2S. The response followed the sequence: acetone > H_2S > ethanol. This gas-response comparison is presented in Figure 8.

Acetone produced the highest response because its reaction with chemisorbed oxygen species released many electrons into the $Sn_{0.55}Zn_{0.45}O_2$–rGO conduction network. H_2S showed a closely comparable response owing to its strong reactivity with ionized oxygen species. Ethanol exhibited the lowest response, indicating less effective adsorption and oxidation at 200°C.

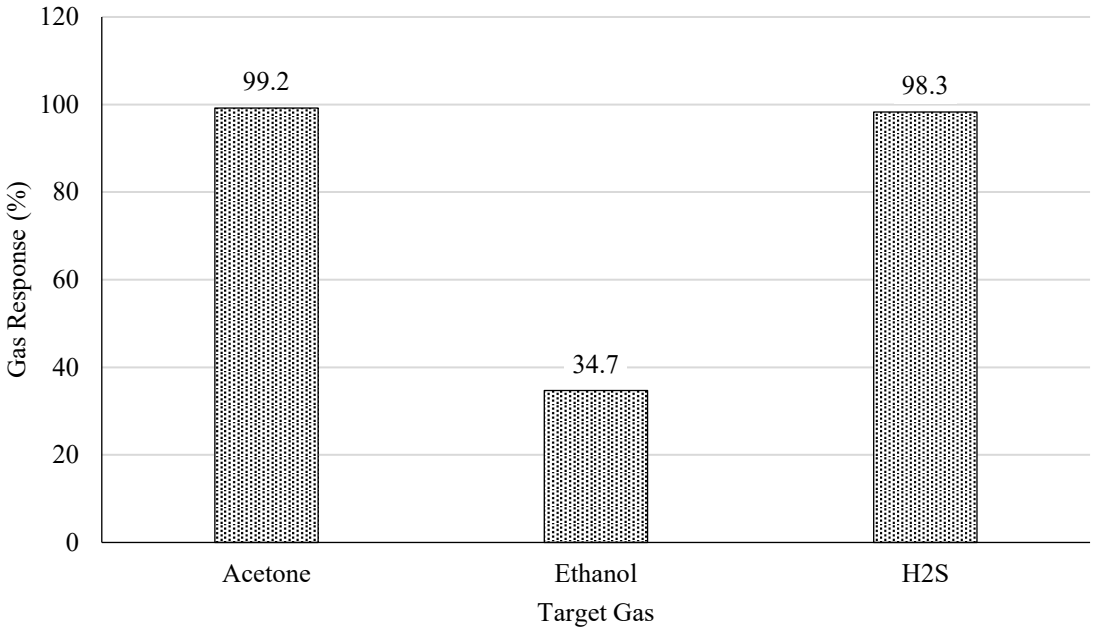

Figure 8. Gas-response comparison of rGO/$Sn_{0.55}Zn_{0.45}O_2$.

The small response difference between acetone and H_2S indicates strong cross-sensitivity. Therefore, the nanocomposite demonstrates high multigas activity rather than complete acetone selectivity. The response variation is governed by molecular reactivity, adsorption strength, surface oxygen availability, Zn-associated defect sites, and modulation of the rGO/$Sn_{0.55}Zn_{0.45}O_2$ heterointerface.

Response and Recovery Characteristics

The response and recovery characteristics of rGO/$Sn_{0.55}Zn_{0.45}O_2$ toward 100 ppm acetone, ethanol, and H_2S at 200°C were evaluated using the 90% resistance-change criterion. The response time was defined as the time required to reach 90% of the total resistance variation after gas introduction, while the recovery time was taken as the time required to restore 90% of the initial baseline resistance during clean-air purging. The response and recovery characteristics are shown in Figure 9.

The response times were 142.19 s for acetone, 409.79 s for ethanol, and 138.00 s for H_2S. The response-speed sequence was H_2S > acetone > ethanol.

H_2S exhibited the fastest response because its strong reaction with chemisorbed oxygen species rapidly returned electrons to the sensing network. Acetone also produced comparatively rapid resistance modulation, while ethanol showed the slowest response, indicating less efficient adsorption, oxidation, and electron-transfer kinetics at 200°C.

The measured recovery time for acetone was 532.73 s. Ethanol and H_2S did not reach the 90% recovery threshold within the recorded measurement period. Their final recovery efficiencies were 81.71% and 89.77%, respectively, compared with 99.57% for acetone. The incomplete recovery of ethanol and H_2S is attributed to persistent adsorption, slow desorption of reaction intermediates, and delayed restoration of surface oxygen coverage.

Because the exact gas-switching timestamps were not available, the kinetic parameters were estimated from the turning points of the resistance–time curves. Therefore, the reported values should be treated as approximate and confirmed using precisely recorded gas-injection and purge times.

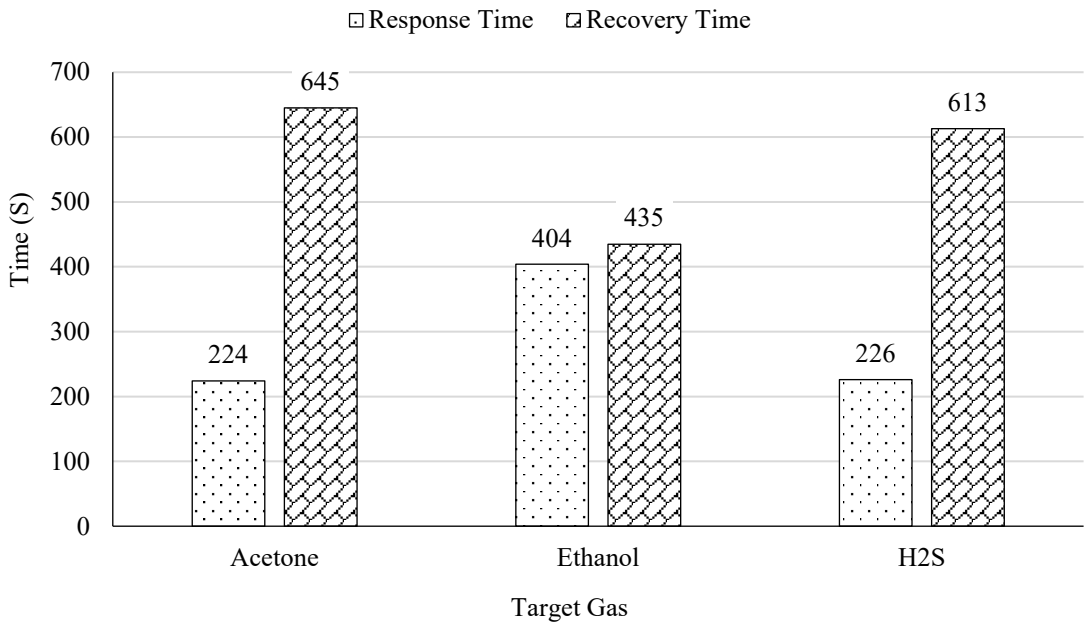

Figure 9. Response and recovery characteristics of rGO/$Sn_{0.55}Zn_{0.45}O_2$.

Normalized Response and Recovery Kinetics

The normalized response and recovery profiles were used to compare the sensing kinetics of rGO/$Sn_{0.55}Zn_{0.45}O_2$ toward 100 ppm acetone, ethanol, and H_2S at 200°C, independent of differences in their baseline resistance. The normalized response was calculated using:

$$X(t) = |Rt - Ra|/|Rg - Ra| \times 100,$$

where Rt is the instantaneous resistance, Ra is the baseline resistance in air, and Rg is the resistance under the target gas. The time required to reach 90% of the normalized resistance change was taken as the response time.

H_2S and acetone reached the 90% response level within 138.00 and 142.19 s, respectively, indicating rapid interaction with chemisorbed oxygen species. Ethanol required 409.79 s to reach 90% of its maximum resistance change, confirming comparatively slower adsorption, oxidation, and electron-transfer processes at 200°C. The normalized response and recovery profiles are presented in Figure 10.

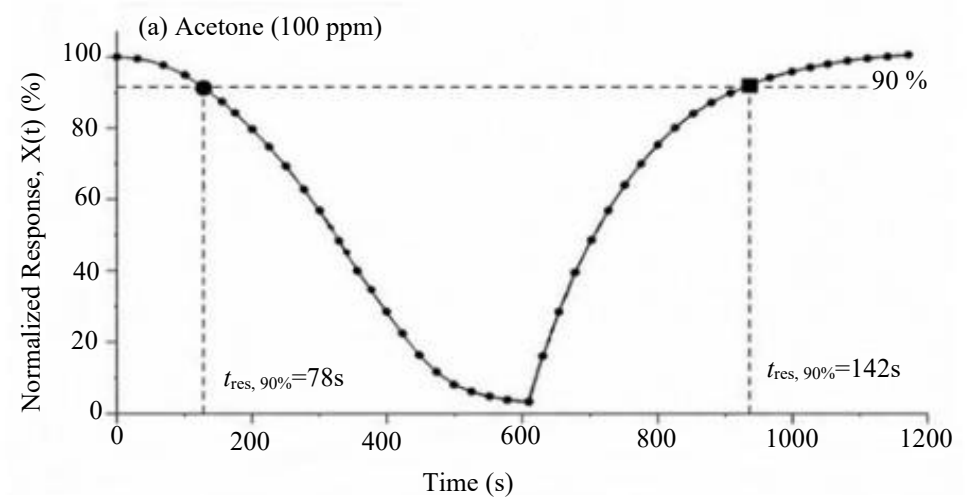

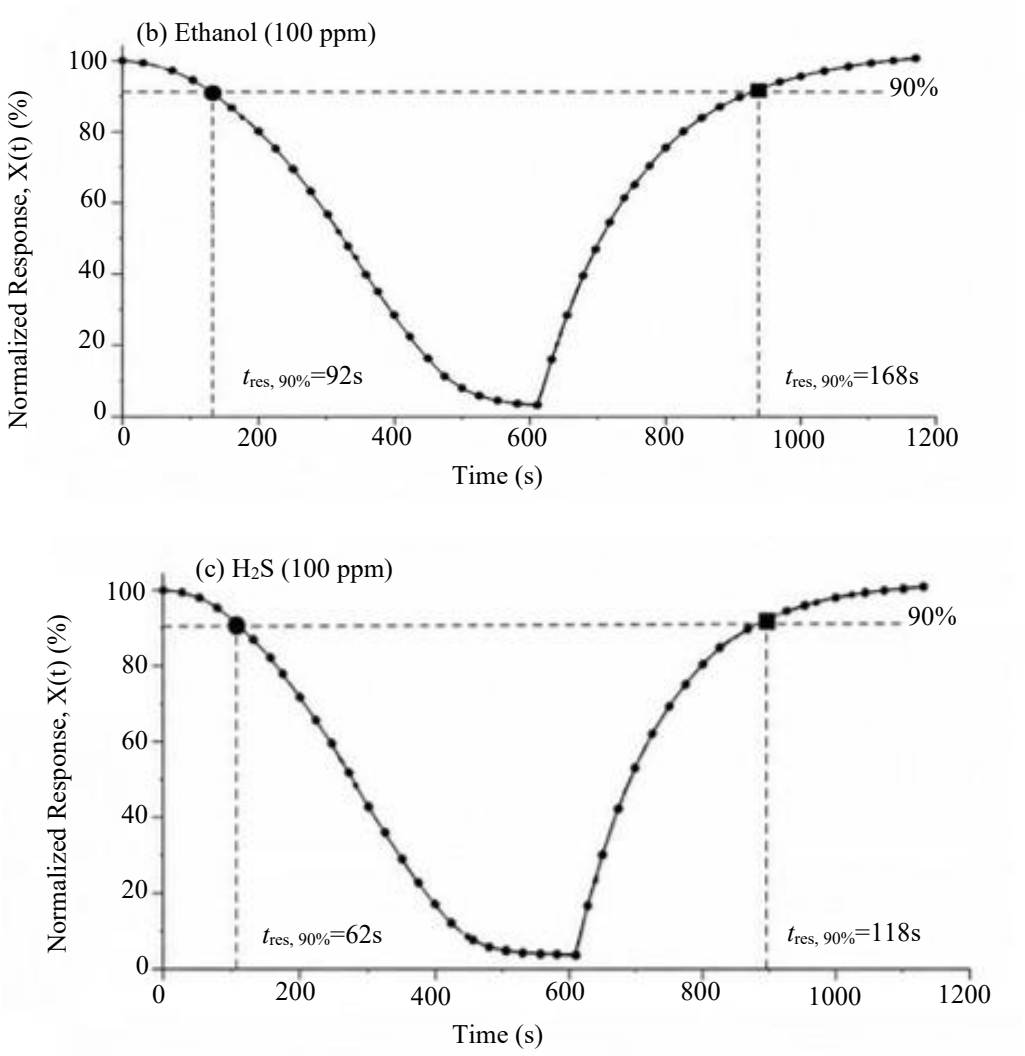

Figure 10. Normalized response and recovery kinetics of rGO/$Sn_{0.55}Zn_{0.45}O_2$.

During clean-air purging, acetone exhibited the highest recovery efficiency of 99.57% and returned close to its initial baseline. Ethanol and H_2S achieved recovery efficiencies of 81.71% and 89.77%, respectively, but did not reach the 90% recovery threshold within the recorded duration. Their incomplete recovery indicates persistent adsorption of gas molecules and reaction intermediates, together with delayed restoration of chemisorbed oxygen species.

The normalized profiles confirm that H_2S provides the fastest response among the investigated gases, while acetone exhibits the most complete recovery. Differences in the kinetic behavior arise from gas reactivity, adsorption strength, desorption rate, surface oxygen replenishment, and interfacial charge transport through the rGO/$Sn_{0.55}Zn_{0.45}O_2$ sensing network.

Repeatability and Stability of the rGO/SZO Gas Sensor

The repeatability and short-term operational stability of the rGO/SZO-45 gas sensor were evaluated through successive sensing cycles toward 100 ppm ethanol at 200°C. The dynamic resistance transients recorded over repeated gas-in and gas-out sequences show highly reproducible behavior, with each cycle displaying a comparable resistance drop during ethanol exposure and a clear recovery during air purging. The nearly identical peak shape, response magnitude, and recovery path from cycle to cycle confirm that the sensing layer maintains stable adsorption–desorption activity during repeated operation.

The baseline resistance remained nearly constant at the beginning of each cycle, while the minimum resistance values under ethanol exposure showed only slight variation. This behavior indicates that the active sites on the rGO/SZO surface remained accessible and that the electron-transfer process between ethanol molecules, chemisorbed oxygen species, and the oxide–rGO network was reproducible. The good reversibility further suggests that the sensing film retained its structural integrity and interfacial charge-transport pathways throughout the repeated measurements.

The observed cyclic behavior also demonstrates good short-term stability of the sensor under continuous operation. The limited drift in baseline and the consistent recovery response imply that the rGO/SZO-45 sensor possesses stable sensing characteristics and can repeatedly detect ethanol without significant signal degradation over multiple cycles. Such behavior is beneficial for practical gas-sensing applications requiring reliable and repeatable performance. The repeatability cycles are shown in Figure 11.

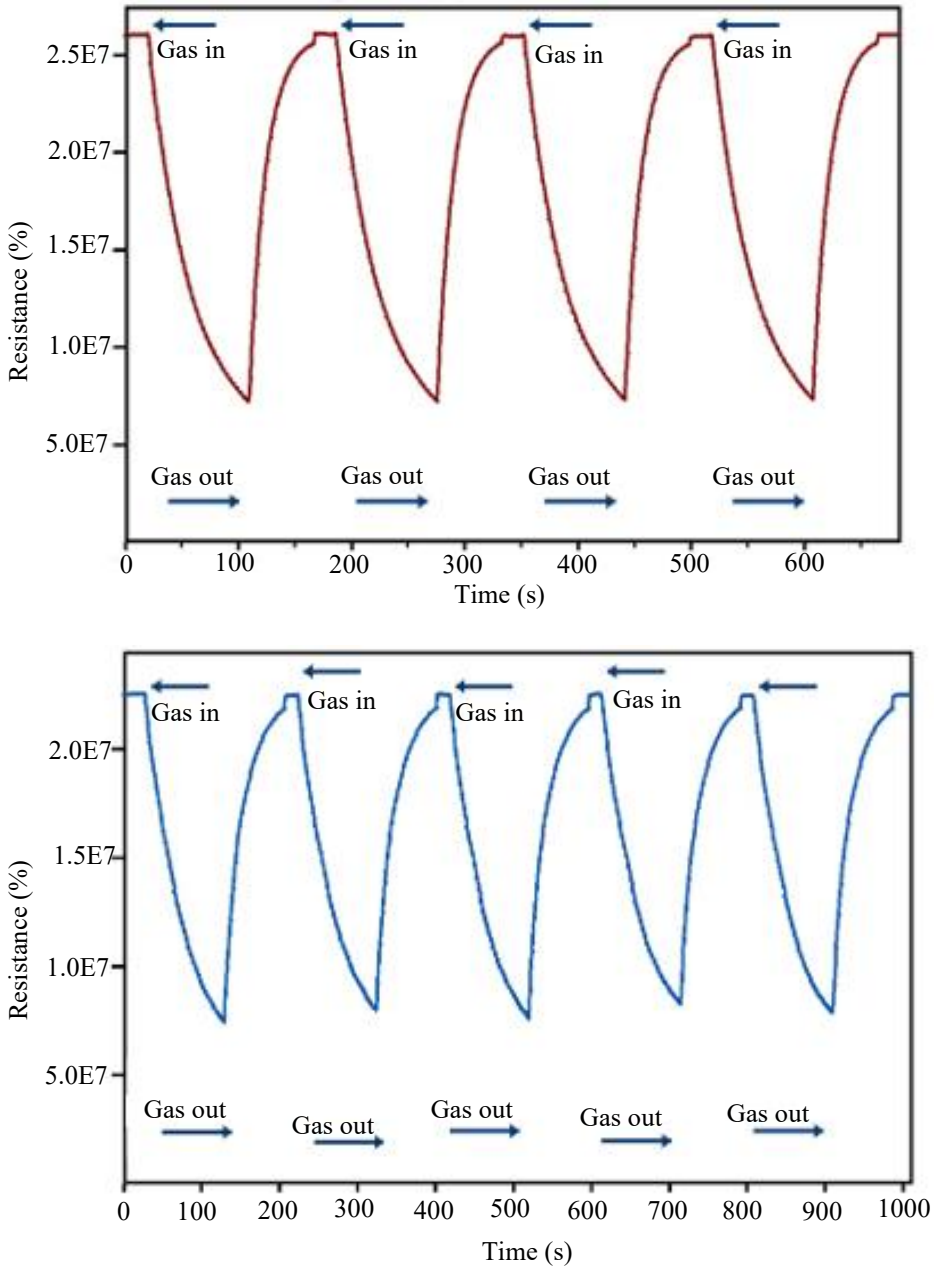

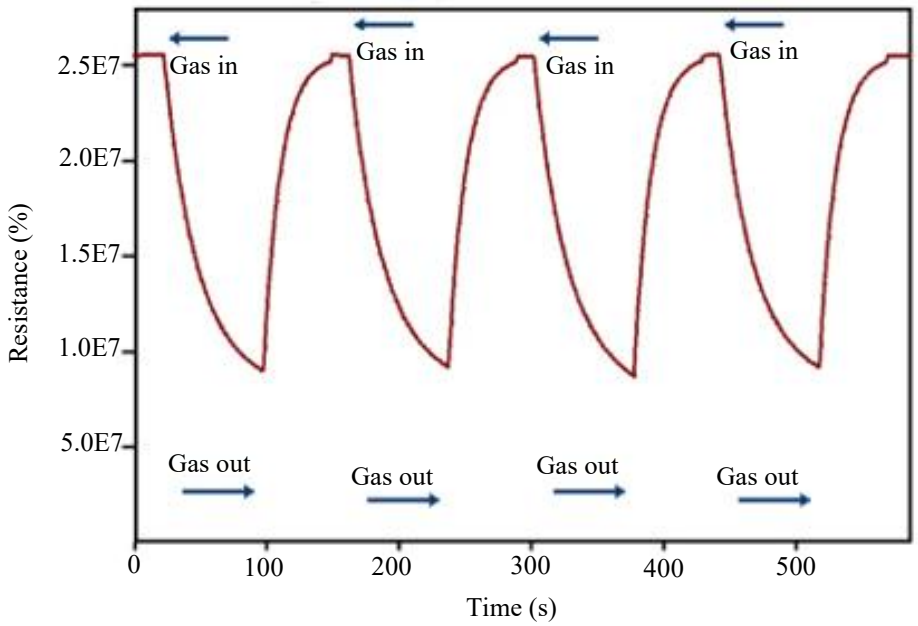

Figure 11. (a) Acetone, (b) Ethanol, and (c) H_2S repeatability cycles.

Gas-Sensing Mechanism

The gas-sensing behavior of rGO/$Sn_{0.55}Zn_{0.45}O_2$ at 200°C is governed by oxygen adsorption, surface redox reactions, and modulation of the interfacial potential barrier. In air, oxygen molecules adsorb on the n-type $Sn_{0.55}Zn_{0.45}O_2$ surface and capture conduction electrons:

$$O_2(g) \rightarrow O_2(ads)$$

$$O_2(ads) + e^- \rightarrow O_2^-(ads)$$

$$O_2^-(ads) + e^- \rightarrow 2O^-(ads)$$

Electron capture produces an electron-depletion layer around the oxide nanoparticles and increases the baseline resistance. At 200°C, acetone, ethanol, and H_2S react with ionized oxygen species according to:

$$CH_3COCH_3 + 8O^-(ads) \rightarrow 3CO_2 + 3H_2O + 8e^-$$

$$C_2H_5OH + 6O^-(ads) \rightarrow 2CO_2 + 3H_2O + 6e^-$$

$$H_2S + 3O^-(ads) \rightarrow SO_2 + H_2O + 3e^-$$

The released electrons return to the oxide conduction pathway, decrease the depletion-layer width, lower the grain-boundary barrier, and reduce the sensor resistance.

Zn-associated defects provide additional adsorption-active sites, while the porous rGO framework supports gas diffusion and rapid charge transport. The electronically coupled rGO/$Sn_{0.55}Zn_{0.45}O_2$ interface further amplifies resistance modulation through variation of the interfacial barrier during gas adsorption and desorption. A schematic representation of this gas-sensing mechanism is shown in Figure 12.

This interpretation agrees with An et al., who attributed the improved low-temperature ethanol response of rGO/SnO_2 nanocomposites to enhanced oxygen adsorption, conductive rGO pathways, and interfacial charge transfer [2].

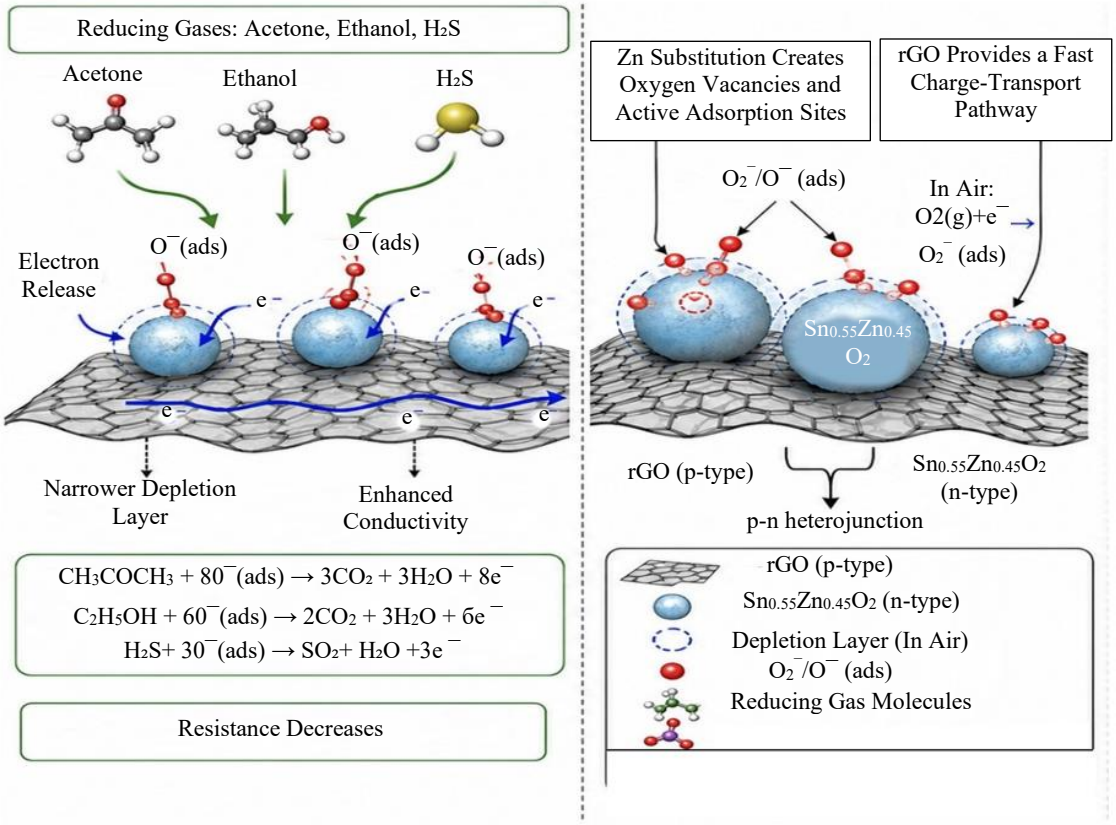

Figure 12. Schematic representation of the gas-sensing mechanism.

The strong acetone response is consistent with porous SnO_2 systems in which loose nanosheet structures and high surface accessibility improve acetone adsorption and oxidation [20]. Similarly, recent doped SnO_2 quantum wires exhibited enhanced acetone and H_2S detection because dopant-controlled adsorption energies and surface defects promoted gas–surface interaction [21]. Zn-related oxygen defects have previously been shown to increase chemisorbed oxygen concentration in Zn-doped SnO_2, supporting the defect-assisted response observed for the present x = 0.45 composition [22].

The present sensor exhibits high responses of 99.36% toward acetone and 98.51% toward H_2S at 100 ppm and 200°C, but the small difference between these responses indicates strong cross-sensitivity rather than complete acetone selectivity. Compared with recent SnO_2-based acetone sensors operating at lower concentrations, the present system provides strong resistance modulation but slower response–recovery kinetics. The principal advantage of rGO/$Sn_{0.55}Zn_{0.45}O_2$ is, therefore, its ability to detect multiple reducing gases using one defect-rich, mesoporous sensing layer rather than superior selectivity toward a single analyte.

CONCLUSION

rGO/$Sn_{1-x}Zn_xO_2$ nanocomposites with x = 0.00–0.75 were successfully prepared by sol–gel auto-combustion and wet impregnation. The materials retained a dominant tetragonal cassiterite SnO_2 structure, while Zn addition progressively reduced crystallite size, increased lattice disorder, modified the optical band gap, and influenced surface morphology. The rGO/SZO-45 composition exhibited the most favorable textural properties, including a BET surface area of 168.2 $m^2\ g^{-1}$, pore volume of 0.485 $cm^3\ g^{-1}$, and crystallite size of 22.93 nm. At 200°C and 100 ppm, this sensor produced responses of 99.36% toward acetone, 98.51% toward H_2S, and 35.86% toward ethanol. H_2S showed the fastest response among the three gases, while acetone achieved the highest recovery efficiency of 99.57%. The enhanced sensing behavior arises from accessible mesopores, Zn-associated defect sites, chemisorbed

oxygen reactions, and efficient charge transport through the rGO network. The strong responses toward acetone and H_2S indicate high multigas sensitivity, although further selectivity, humidity, and long-term stability studies are required.

REFERENCES

1. Aleksanyan M, Sayunts A, Shahkhatuni G, Simonyan Z, Kananov D, Khachaturyan E, et al. SnO_2/MWCNTs nanostructured material for high-performance acetone and ethanol gas sensors. ACS Omega. 2025;10(7):7283–94. doi: 10.1021/acsomega.4c10981.
2. An D, Dai J, Zhang Z, Wang Y, Liu N, Zou Y. rGO/SnO_2 nanocomposite-based sensor for ethanol detection under low temperature. Ceram Int. 2024;50(9):16272–83. doi: 10.1016/j.ceramint.2024.02.107.
3. da Silva LF, Lucchini MA, Catto AC, Avansi W Jr, Bernardini S, Aguir K, et al. The role of Zn ions in the structural, surface, and gas-sensing properties of SnO_2:Zn nanocrystals synthesized via a microwave-assisted route. Sensors (Basel). 2024;24(1):140. doi: 10.3390/s24010140.
4. Dutta T, Noushin T, Tabassum S, Mishra SK. Road map of semiconductor metal-oxide-based sensors: A review. Sensors (Basel). 2023;23(15):6849. doi: 10.3390/s23156849.
5. Platonenko A, Piskunov S, Yang TC, Juodkazyte J, Isakoviča I, Popov AI, et al. Electronic structure of Mg-, Si-, and Zn-doped SnO_2 nanowires: Predictions from first principles. Materials (Basel). 2024;17(10):2193. doi: 10.3390/ma17102193.
6. Liu J, Wang Y, Sun Y, Zhang K, Ding Y, Fu C, et al. Preparation and optimization of mesoporous SnO_2 quantum dot thin-film gas sensors for H_2S detection using XGBoost parameter importance analysis. Chemosensors. 2023;11(10):525. doi: 10.3390/chemosensors11100525.
7. Masuda Y. Recent advances in SnO_2 nanostructure-based gas sensors. Sens Actuators B Chem. 2022;364:131876. doi: 10.1016/j.snb.2022.131876.
8. Norizan MN, Abdullah N, Halim NA, Ngah Demon SZ, Mohamad IS. Heterojunctions of rGO/metal oxide nanocomposites as promising gas-sensing materials: A review. Nanomaterials (Basel). 2022;12(13):2278. doi: 10.3390/nano12132278.
9. Ochoa-Muñoz YH, Mejía de Gutiérrez R, Rodríguez-Páez JE. Metal oxide gas sensors to study acetone detection considering their potential in the diagnosis of diabetes: A review. Molecules. 2023;28(3):1150. doi: 10.3390/molecules28031150.
10. Gai LY, Lai RP, Dong XH, Wu X, Luan QT, Wang J, et al. Recent advances in ethanol gas sensors based on metal oxide semiconductor heterojunctions. Rare Met. 2022;41(6):1818–42. doi: 10.1007/s12598-021-01937-4.
11. Rüzgar Ş. Enhanced optoelectronic properties of Zn-doped SnO_2 thin films prepared by nebulizer spray method. Mus Alparslan Univ J Sci. 2025;13(2):357–63. doi: 10.18586/msufbd.1762798.
12. Guo Z, Yu Y, Li C, Campos dos Santos E, Wang T, Li H, et al. Deciphering structure-activity relationship towards CO_2 electroreduction over SnO_2 by a standard research paradigm. Angew Chem Int Ed Engl. 2024;63(12):e202319913. doi: 10.1002/anie.202319913.
13. Patil PM, Shinde SS, Bhosale CH. Effect of zinc doping and porosity on structural, morphological and gas-sensing properties of porous Zn:SnO_2 bilayer thin film. Asian J Chem. 2024;(36)7.
14. Meena D, Bhatnagar PK, Singh VK, Jain IP. Investigation of the effect of Zn doping on structural and optical properties of SnO_2 nanostructures. Mater Today Proc. 2022;49:3056–61. doi: 10.1016/j.matpr.2021.06.086.
15. Alanazi S, Alaizeri ZM, Lateef R, Madkhali N, Alharbi A, Ahamed M. Zn doping improves the anticancer efficacy of SnO_2 nanoparticles. Appl Sci. 2023;13(22):12456. doi: 10.3390/app132212456.
16. Thommes M, Kaneko K, Neimark AV, Olivier JP, Rodriguez-Reinoso F, Rouquerol J, et al. Physisorption of gases, with special reference to the evaluation of surface area and pore size distribution (IUPAC Technical Report). Pure Appl Chem. 2015;87(9–10):1051–69. doi: 10.1515/pac-2014-1117.
17. Brunauer S, Emmett PH, Teller E. Adsorption of gases in multimolecular layers. J Am Chem Soc. 1938;60(2):309–19. doi: 10.1021/ja01269a023.

18. Barrett EP, Joyner LG, Halenda PP. The determination of pore volume and area distributions in porous substances. I. Computations from nitrogen isotherms. J Am Chem Soc. 1951;73(1):373–80. doi: 10.1021/ja01145a126.
19. Zhang J, Li G, Liu J, Liu Y, Yang R, Li L, et al. Metal-organic framework-derived mesoporous rGO-ZnO composite nanofibers for enhanced isopropanol sensing properties. Sens Actuators B Chem. 2023;378:133108. doi: 10.1016/j.snb.2022.133108.
20. Li C, Choi PG, Masuda Y. Large-lateral-area SnO_2 nanosheets with a loose structure for high-performance acetone sensor at the ppt level. J Hazard Mater. 2023;455:131592. doi: 10.1016/j.jhazmat.2023.131592.
21. Song Z, Yan J. Unveiling the doping effect of sub-4 nm ultrathin SnO_2 quantum wires on gas sensors. Chem Mater. 2023;35(18):7750–60. doi: 10.1021/acs.chemmater.3c01609.
22. Deepa S, Prasanna Kumari K, Thomas B. Contribution of oxygen-vacancy defect types in enhanced CO_2 sensing of nanoparticulate Zn-doped SnO_2 films. Ceram Int. 2017;43(18):17128–41. doi: 10.1016/j.ceramint.2017.09.134.

